The Mesoscale and Microscale Structure and Organization of Clouds and Precipitation in Midlatitude Cyclones. III: Air Motions and Precipitation Growth in a Warm-Frontal Rainband

ROBERT A. HOUZE, JR., STEVEN A. RUTLEDGE, THOMAS J. MATEJKA[1] AND PETER V. HOBBS

Department of Atmospheric Sciences,[2] University of Washington, Seattle 98195

(Manuscript received 2 July 1980, in final form 17 November 1980)

ABSTRACT

Doppler radar data and airborne cloud microphysical measurements obtained in the CYCLES PROJECT indicate that a warm-frontal rainband in an extratropical cyclone was characterized by a precipitation process in which clouds at low levels were enhanced by a mesoscale updraft. Ice particles, apparently formed in shallow convective cells aloft and then drifted downward, undergoing aggregation just above the melting layer. This study demonstrates the crucial role of the low-level mesoscale updraft in condensing a sufficient amount of cloud water for particles to accrete as they fell through the lower portion of the frontal cloud.

1. Introduction

This paper is the third in a series dealing with the mesoscale structure of clouds and precipitation in extratropical cyclones moving into Washington State from the Pacific Ocean. In Part I of the series, Hobbs *et al.* (1980) described the mesoscale rainbands associated with a well-defined cold front. In Part II, Herzegh and Hobbs (1980) examined rainbands in warm-frontal regions of cyclones. The present paper is a further examination of warm-frontal rainbands.

Warm-frontal rainbands may be described as mesoscale features within which the widespread precipitation associated with the warm advection and general upward motion of a cyclone is enhanced. Widespread frontal precipitation is characterized in general by ice particles forming aloft and growing as they drift downward toward a well-defined melting level. The formation of the ice particles often occurs in a layer of shallow convective "generating cells", from which trail long sloping streamers of snow that form distinctive radar echo patterns (Battan, 1973, pp. 195–197). Such cells are particularly notable in the vicinities of warm-frontal rainbands and evidently play a role in enhancing the precipitation in those regions. Houze *et al.* (1976b) and Hobbs and Locatelli (1978) showed that most of the growth of the precipitation particles occurs below the layer containing the cells. Herzegh and Hobbs (1980), using observed vertical profiles of radar reflectivity, quantified this result, showing that 80% of the growth of precipitation particles occurred after they fell out of generating cells. Direct sampling of the precipitation particles in warm-frontal rainbands shows that a primary growth mechanism as the particles approach the melting level is aggregation (Matejka *et al.*, 1980). Herzegh and Hobbs (1980) showed that the falling particles also grow by scavenging smaller cloud droplets in their paths both before and after they pass through the melting layer.

These results indicate that the shallow convective cells aloft do not by themselves increase the precipitation from the clouds associated with warm-frontal rainbands. Rather, most of the mass of the precipitation particles is acquired as they fall through lower level stratiform cloud. The ice particles from the cells aloft thus aid in the microphysical *conversion* of cloud water condensed at lower levels to precipitation, while the *condensation* of water vapor in the lower cloud provides the mass of water accrued by the falling ice particles.

Herzegh and Hobbs (1980) found a mesoscale region of enhanced lifting in the lower cloud layers associated with one of the warm-frontal rainbands they studied. This result suggests that mesoscale lifting at low levels was dynamically enhancing the condensation of water vapor, thus producing a thick, water-laden cloud.

It thus appears from previous studies that the enhancement of the precipitation in warm-frontal rainbands may result from: 1) generation of "seeder" crystals aloft, which as they fall out, increase the

[1] Present affiliation: Department of Geophysical Sciences, University of Chicago.

[2] Contribution No. 555, Department of Atmospheric Sciences, University of Washington.

0022-4928/81/030639-11$06.75

microphysical conversion of "feeder" cloud water condensed at lower levels to precipitation water; 2) enhanced mesoscale lifting, which increases the amount of feeder cloud water by the condensation of vapor at low levels; or 3) a combination of both of these mechanisms.

In the present study, we confirm in a case study that both mechanisms occur in combination and that the mesoscale lifting at low levels is crucial in accounting for the amount of rain associated with a warm frontal rainband.

2. Data

The data used in this study were obtained on 13 December 1977 as part of the CYCLES PROJECT of the University of Washington. A complete description of the observational facilities is given in Part I (Hobbs *et al.*, 1980).

3. Methods of air motion computation

Two methods of deriving the air motion pattern within the rainband have been applied in this study. Method I is used to derive the air motion pattern in a vertical plane that is perpendicular to the rainband. This two-dimensional air motion pattern is derived from the CP-3 Doppler velocity measurements. Coordinates are x, horizontal and normal to the band, and height z. The horizontal wind in the x direction is u. An isotach analysis of u determined from the radar data was then performed in the x-z plane and values of u in a Cartesian grid were interpolated. A horizontal spacing of 2.60 km and vertical spacing of 0.33 km was used. The horizontal divergence, $\Delta u/\Delta x$, was calculated for the entire field. A value of Δx of 5.2 km was used. It was assumed that the divergence of the horizontal wind v along the rainband, that is in a direction y, normal to the x-z plane, is small compared to $\Delta u/\Delta x$. The two-dimensional continuity equation

$$\frac{\Delta \omega}{\Delta p} = -\frac{\Delta u}{\Delta x}, \tag{1}$$

where p is pressure and ω ($\equiv dp/dt$) the vertical velocity, was integrated to obtain ω at 0.33 km intervals in the vertical. A lower boundary condition of no vertical motion was used, and p and z were used interchangeably assuming they were related hydrostatically by $\delta p = -\rho g \delta z$, where g is the acceleration of gravity and ρ the density, given by $\rho_0 \exp(-z/H)$, where ρ_0 is the surface density and H the scale height.

Method II for deriving air motions from Doppler radar measurements is the "velocity-azimuth display" (VAD) technique of Browning and Wexler (1968) in which a Fourier series is used to represent an azimuthal sequence of radial velocity measurements obtained at a given range and elevation angle. Kinematic properties of the horizontal wind field, such as average speed and direction, divergence, deformation and orientation of the axis of dilatation, are determined for the circular region defined by the range and elevation angle by various algebraic combinations of the Fourier coefficients. Using this technique, we calculated the divergence for eight levels in the vertical, and the continuity equation was used to calculate the corresponding vertical velocity profile, with no vertical motion applied as the lower boundary condition.

Browning and Wexler's technique for computing the divergence requires knowledge of the particle fallspeed $\bar{v}_f$. We obtained values of $\bar{v}_f$ of about 7 m s^{-1} from measurements taken when the Doppler radar was pointing vertically.

From VAD data, both components of the divergence, $\partial u/\partial x$ and $\partial v/\partial y$, can be computed. By examining the values of these components, we determined the validity of the two-dimensional assumption used in Method I.

To minimize VAD errors owing to partial filling of the VAD circle by detectable precipitation, spatial variability of particle fallspeeds and strong vertical wind shear, we have restricted the elevation angle to a maximum of 9° and the radius of the VAD circle to a maximum of 9 km in all our calculations. Hills or other terrain features did not affect these measurements and calculations since within 9 km range of the radar 80% of the region covered was ocean and the remaining 20% extremely low and flat land.

4. Horizontal patterns

The frontal cloud pattern detected by satellite at the time of our study, 1130–1230 PST, was quite typical of cylones moving into Washington State from the Pacific Ocean (Fig. 1a). The precipitation pattern revealed by radar is shown in the inset. The National Weather Service's surface map analysis (Fig. 1b) shows the frontal pattern as it was moving onshore just after the time of our detailed observations. The airflow at 500 mb a short time later is shown in Fig. 1c.

The rainband studied in detail here is that labeled 3 in the inset of Fig. 1a. A switch in orientation occurred between the leading rainbands 1–3 and the trailing rainbands 4–8. This change in rainband orientation is rather typical of this type of cyclonic storms. Houze *et al.* (1976b) used such changes in orientation to classify rainbands into various types. According to their classification, the first group of rainbands (1–3) are considered "warm-frontal" rainbands. Rainband 3 was the last of the warm-frontal rainbands associated with this cyclone to pass through the area of study.

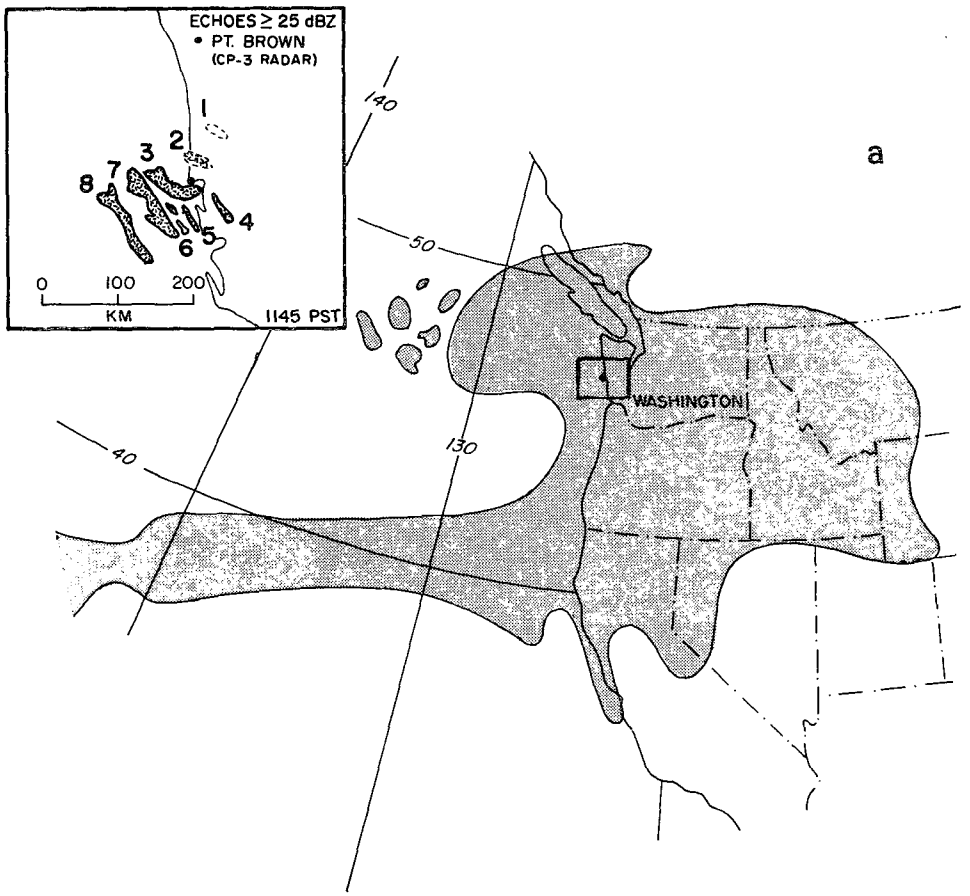

FIG. 1a. Satellite view of the clouds associated with the frontal positions at 1145 LST. Shaded area was traced from infrared imagery. The inset represents an expanded view of the hatched rectangle showing a composite of the horizontal patterns of the precipitation (radar echoes ≥ 25 dBZ) comprising rainbands 1–8.

5. Radar reflectivity cross section

Figure 2 shows a vertical cross section of the radar reflectivity pattern associated with the rainband. A pronounced melting layer, indicated by the band of high reflectivity at ~2 km, emphasizes the basically stratiform structure of the precipitation in the rainband. Had convective-scale updrafts and downdrafts been present to any considerable extent at the height of the melting layer, the melting band would have been irregular, discontinuous or completely obscured. Above 3 km, the radar echo was much less stratiform. The three perturbations of the 24 dBZ echo contour had the appearance of precipitation trails from generating cells. This impression is affirmed by data from aircraft penetrations at the 3, 4 and 5 km levels (see Section 9).

The horizontally uniform structure below the trails from the generating cells in Fig. 2 is consistent with previous studies in which aircraft penetrations below the level of generating cells in the clouds associated with warm-frontal rainbands have revealed generally uniform structures with no evidence of convective activity (Houze *et al.*, 1976a; Matejka *et al.*, 1980).

6. Divergence

The quantity $\Delta u/\Delta x$ computed by Method I from the Doppler velocity data for 1130 LST is shown in the x-z plane in Fig. 3a. To the extent that the rainband is two-dimensional, this quantity is equal to the divergence of the horizontal wind. Fig. 3a and all subsequent figures involving air motion fields calculated by Method I show values only within the boundary of the 34 dBZ echo contour. The Doppler velocities obtained outside this contour were characterized by unrealistic vertical wind shears and were therefore considered unreliable.

At low levels (below 2 km), the values of $\Delta u/\Delta x$ were all in the range of -2×10^{-4} to -5×10^{-4} s^{-1}. This pattern extends continuously across the rainband, showing that the lower 2 km of the cloud associated with the rainband coincided with a meso-

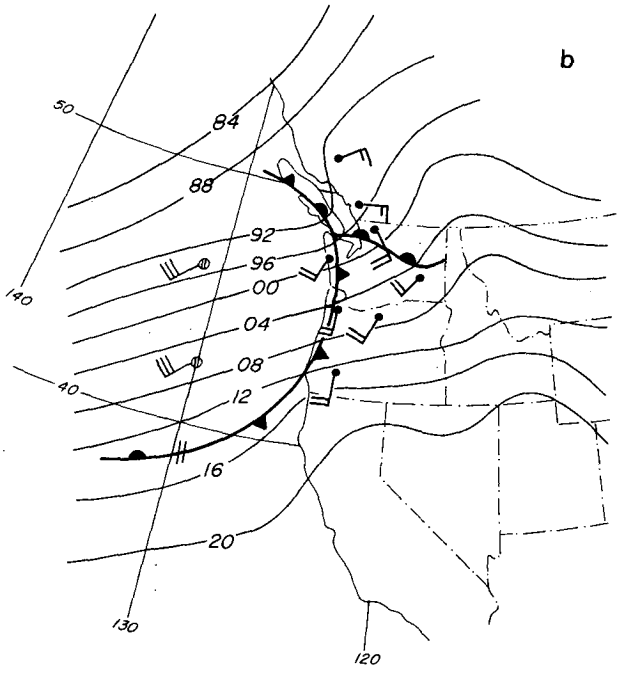

FIG. 1b. National Weather Service surface analysis for 1300 LST 13 December 1977, showing isobars and frontal positions along the west coast of the United States.

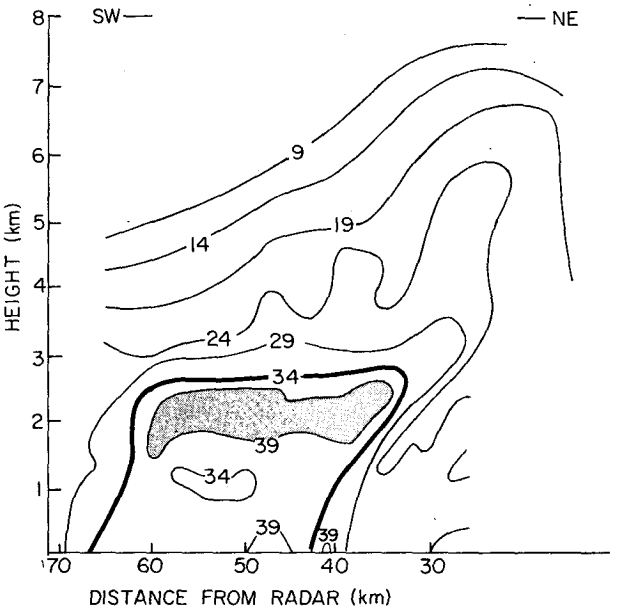

FIG. 2. Radar reflectivity patterns (dBZ) in a vertical plane perpendicular to the warm-frontal rainband. The data were taken along the 212° radial (from Pt. Brown, Washington) at 1130 LST 13 December 1977.

scale region of rather uniform convergence. Near the back edge of the rainband (60 km from the radar), the region of convergence extended upwards to the top of the echo. The middle portion of the echo is dominated by divergence of a magnitude similar to that of the convergence.

At 1200 LST, the rear portion of the band was centered over the radar, and the VAD method could therefore be applied in the region indicated by the dashed line in Fig. 3a. Profiles of the divergence components obtained for this region are shown in Fig. 3b. The $\partial u/\partial x$ term is dominant, ranging from -5×10^{-4} s^{-1} at the surface to -1×10^{-4} s^{-1} at 1.5 km. These values are highly consistent with those in the dashed region in Fig. 3b. These results support the validity of the two-dimensional approximation used in Method I.

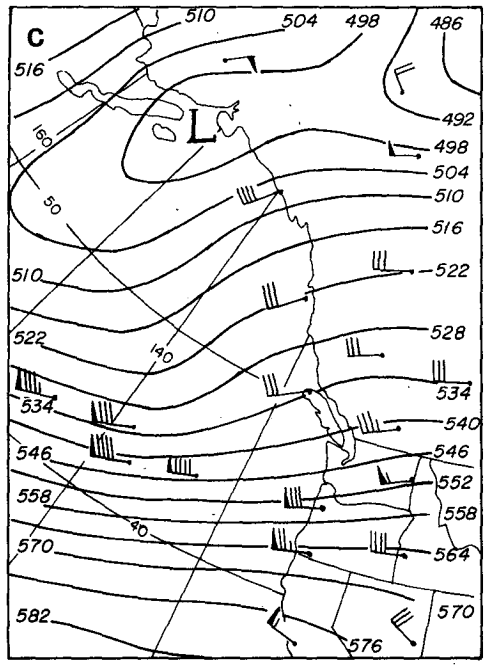

FIG. 1c. National Weather Service 500 mb analysis for 1600 LST 13 December 1977. Solid lines indicate the 500 mb height (dam).

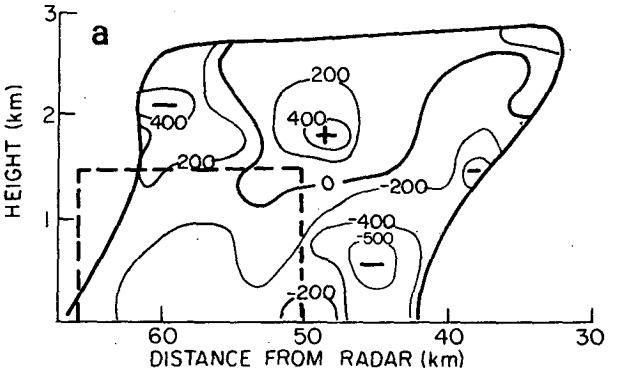

FIG. 3a. Pattern of $\Delta u/\Delta x$ (in units of 10^{-6} s^{-1}) in the warm-frontal rainband calculated by Method I. Outside boundary is the 34 dBZ contour. The dashed line represents the region where the VAD analysis was performed.

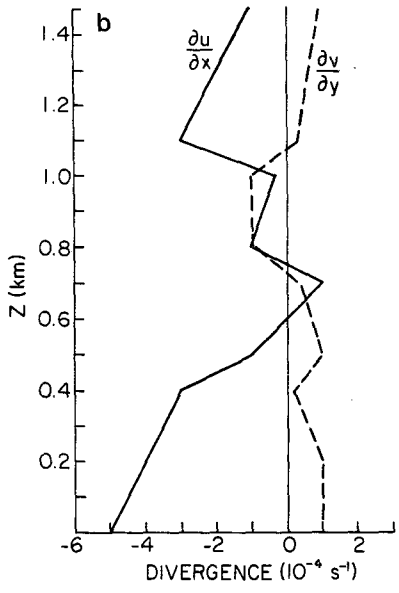

FIG. 3b. Vertical profiles of $\partial u/\partial x$ and $\partial v/\partial y$ in the warm-frontal rainband calculated from Method II. Values represent the average divergence over a circle of radius 9 km.

7. Vertical velocity

The vertical velocity w, computed from the $\Delta u/\Delta x$ field in Fig. 3a using (1), was upward throughout the rainband echo, with magnitudes of tens of centimeters per second (Fig. 4a). The entire rainband below the 3 km level may, therefore, be regarded as a mesoscale upward motion feature. As noted in discussing Fig. 2, convective cells were evidently located above the 3 km level. The vertical velocity profile calculated by the VAD method (Fig. 4b) is in excellent agreement with the vertical velocity calculated by Method I for the region bounded by the dashed line in Fig. 4a. For example, within the dashed region, the average vertical velocity at the same level in Fig. 4b is 28 cm s^{-1}. Because of the excellent agreement of the vertical velocities computed by two independent sets of measurements (obtained 30 min apart), we feel the vertical velocities computed by both methods are accurate.

8. Surface pressure

The region of enhanced vertical velocity and convergence associated with the rainband extended down into the planetary boundary layer (lowest 1 km). Convergence and vertical motion in the boundary layer are associated with cross-isobaric flow. Hence, a mesoscale perturbation in the surface pressure field may be expected to accompany the mesoscale perturbation in divergence and vertical velocity. Mesoscale perturbations in pressure associated with rainbands have been noted previously in CYCLES studies (e.g., Houze *et al.*, 1976b). The

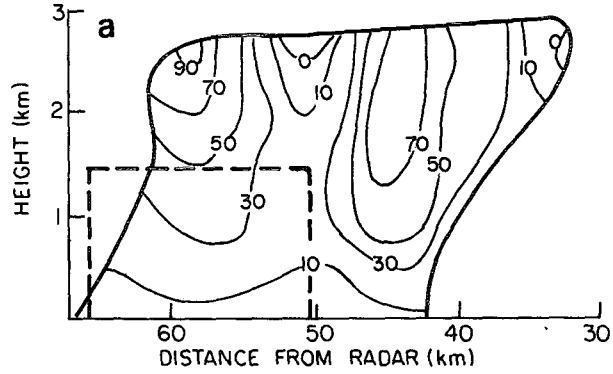

FIG. 4a. Pattern of the vertical velocity (cm s^{-1}) obtained from Method I. Outside boundary is 34 dBZ and the dashed line represents the VAD analysis region.

barograph trace at the radar site showed such a perturbation during the passage of the rainband considered in this study.

Although its applicability to phenomena of the scale of our rainband may be somewhat questionable, Ekman-layer theory may be invoked to estimate the vertical velocity associated with the observed pressure perturbation. The appropriate equation (see Holton, 1972, p. 89) is

$$w_E = \frac{D}{2\pi\rho f}\frac{\partial^2 p}{\partial x^2}, \qquad (2)$$

where w_E is the vertical velocity at the top of the Ekman layer, D the depth of the Ekman layer, and f the Coriolis parameter.

The value of $\partial^2 p/\partial x^2$ associated with the passage of the rainband was estimated from the barograph trace shown in Fig. 5. It is assumed that the dip in

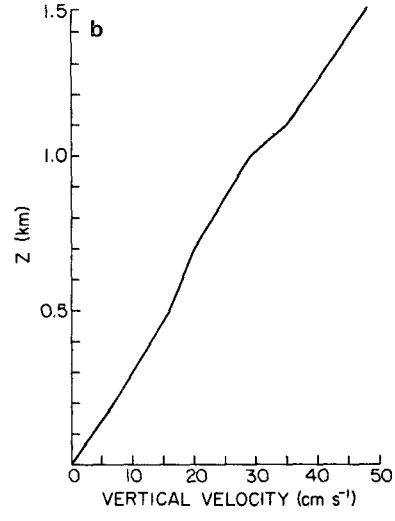

FIG. 4b. Profile of the vertical velocity obtained from Method II. Values represent the average vertical velocity over a circle of radius 9 km.

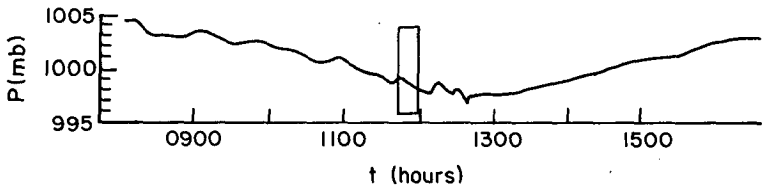

FIG. 5. The barograph trace obtained at Pt. Brown, Washington. The bracketed portion of the trace represents the leading and trailing edge of the warm-frontal rainband passage determined from rainfall records.

the trace centered near the leading edge of the rainband was the pressure perturbation associated with the band. Ideally, the dip would be expected to be centered within the band. The slight misfit of the pressure and precipitation records could be associated with a few minutes uncertainty in timing. The value of $\partial^2 p/\partial x^2$ centered in the dip is estimated to be in the range $2.2-2.6 \times 10^{-3}$ mb km^{-2}. Then, assuming $D = 1$ km, $\rho = 1.15$ kg m^{-3} and $f = 1.07 \times 10^{-4}$ s^{-1}, we obtain a vertical velocity at the 1 km level of 28–34 cm s^{-1}. These values are consistent with the values of w computed from Doppler radar data by both Methods I and II.

9. Airborne observations of cloud and precipitation structure above the melting level

The B-23 aircraft flew northeast–southwest passes through the clouds associated with the rainband at altitudes of 3, 4 and 5 km. These passes were in the region of generating cell streamers evident above the melting level in Fig. 2. Summarized below are the cloud microphysical observations that were obtained on these passes.

a. Ice-particle concentrations and cloud liquid water contents

The ice particle concentrations measured at 5 km (Fig. 6a) were generally high (20–60 per liter). Sharp peaks at 1145, 1147 and 1150 PST evidently corresponded to precipitation streamers of generating cells. The peaks in ice concentration on both the northeast and southwest side of the band coincided with peaks in cloud liquid water content. Since updrafts had to have been present to sustain such liquid water peaks in the presence of ice, we conclude that these observations were obtained within the layer of active convective cellular overturning. Serial rawinsonde ascents ahead of and to the rear of the rainband were not definitive, but did indicate that this layer was probably close to moist adiabatic. The absence of a liquid water peak at 1147 PST suggests that the updraft motion producing this particular streamer had ceased.

At 4 km, observations essentially similar to those at 5 km were obtained (Fig. 6b). Two peaks in ice particle concentration were observed, with one of them (on the northeast side of the band) almost coinciding with a peak in cloud liquid water content, indicating that at 4 km, too, convective updrafts were active.

At 3 km, however, the ice particle concentration, except for the dip at 1108 (Fig. 6c), was spread more uniformly across the rainband, with no sharp peaks. The cloud liquid water content was generally suppressed to values ≤ 0.1 g m^{-3} all across the band. These observations indicate that the aircraft at this level was below the layer of convective overturning and that the streamers from the cells were becoming more diffuse and broadening as they extended downward.

b. Particle replicas

A summary of a careful inspection of the replicas of particles obtained in Formvar on the three penetrations of the clouds associated with the rainband is given in Table 1. The primary findings were the general increase in maximum particle size with decreasing height and the presence of large aggregates of crystals (≥ 3 mm in dimension) at 3 km and the general absence of aggregates at 4 and 5 km. Some riming was noted in all the samples. Evidently, ice particles produced in cells in the 4–5 km layer grew at first by a combination of deposition and riming. As shown by Houghton (1950) deposition probably dominated initially, with riming becoming dominant as the particles' sizes increased. As the streamers extended down into the warmer air at 3 km, aggregation apparently became very important in producing the largest particles. Such a sequence of growth is consistent with the well-known fact that the aggregation of ice particles increases sharply as the ambient temperature increases toward 0°C (Hobbs, 1974, p. 641).

10. Water budget of the rainband

The foregoing radar and aircraft observations may be synthesized by considering the overall water budget of the rainband. Assuming that the rainband was in a steady state and that no evaporation was occurring within its boundaries, the condensation

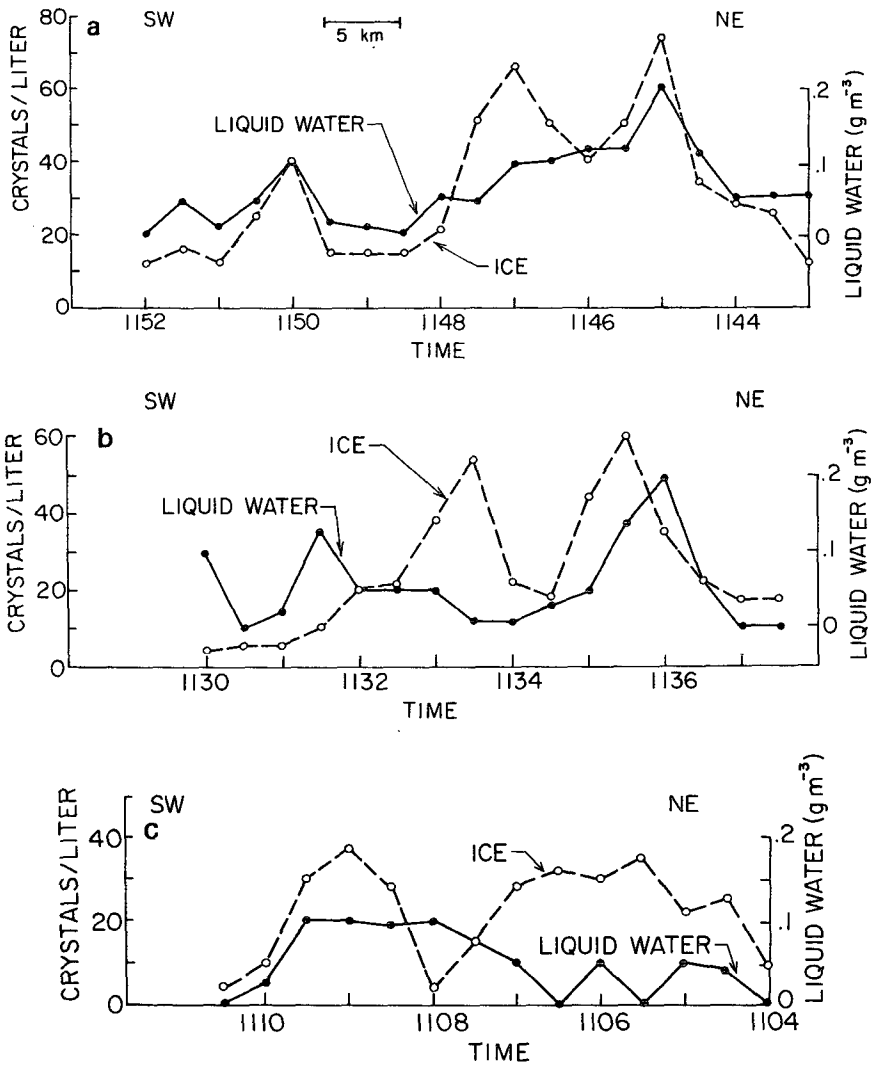

FIG. 6. Liquid water content (solid line) and ice crystal concentrations (dashed line) obtained from aircraft passes. a) Liquid water content (g m^{-3}) and ice crystal concentrations (per liter) along the 5 km altitude pass (−14°C). b) As in Fig. 6a except along the 4 km altitude pass (−8°C). c) As in Fig. 6a except along the 3 km altitude pass (−4°C).

rate C in a volume V of the rainband is given by

$$C = -\iiint_V \nabla\cdot\rho q\mathbf{v}dV = \iint_S \rho q v_n dS, \qquad (3)$$

where $\mathbf{v}$ is the three-dimensional wind vector, q the water vapor mixing ratio, S the surface area of V, v_n the inward directed component of $\mathbf{v}$ across S, and Gauss' theorem has been used to obtain the third expression in (3). C was calculated with both the volume and the surface integrals.

To evaluate the volume integral in C, it is further assumed that the horizontal gradient of q is zero and that the air is saturated. Substitution of the continuity equation for steady-state conditions,

$$\nabla\cdot\rho\mathbf{v} = 0, \qquad (4)$$

and the vector identity,

$$\nabla\cdot\rho q\mathbf{v} = q\nabla\cdot\rho\mathbf{v} + \rho\mathbf{v}\cdot\nabla q, \qquad (5)$$

into the volume integral leads to the expression

$$C = -\iiint_V w\rho\frac{\partial q_s}{\partial z}dV, \qquad (6)$$

where q_s is the saturation mixing ratio.[3]

[3] For a further discussion of the mathematics of describing the water budgets of rainbands, see Hobbs, P. V., and T. J. Matejka, 1980: Precipitation efficiencies and the potential for artificially modifying extratropical cyclones. *Proc. Third WMO Sci. Conf. Weather Modification*, Clermont-Ferrand, France, pp. 9–15.

TABLE 1. Summary of the results of Formvar replication of particles during aircraft penetration of the rainband.

Flight altitude (km)	3	4	5
Temperature (°C)	−4	−8	−14
Sample time (PST)	1106	1132	1147
Particle type	(a) Large aggregates (b) Cloud droplets	(a) Unidentifiable crystals (b) Cloud droplets	(a) Unidentifiable crystals (b) Cloud droplets
Particle size (mm) (μm)	≥ 3 <100	≤ 1 <100	≤ 0.5 <100
Degree of riming	Moderately rimed aggregates	Moderately rimed crystals	Slight
Degree of crystal aggregation	Heavy	Slight	—

We first use (3) and (6) to calculate the condensation rate in the volume of the rainband below 3 km altitude (the region of Doppler radar coverage in Figs. 3–4). The x-z face of the volume V used in (6) is a squared-off version of the 34 dBZ echo contour used to outline the region of Doppler coverage in previous figures. The echo pattern in the cross section is presumed to extend indefinitely in the y direction normal to the x-z plane. We let the volume V extend for a unit length (1 m) in the y direction. Hence, the condensation rate C (kg s^{-1}) is computed for a unit length (1 m) of the band in the y direction. The integrand in (6) is first computed for individual sub-elements of the rainband (Δx = 2.6 km, Δz = 0.33 km, and Δy = 1 m). The resulting field of condensation rate (Fig. 7a) generally follows the pattern of w (Fig. 4a); however, the centers of maximum condensation rate occurred at lower levels than the centers of maximum w because of the strong decrease of the factor $\partial q_s/\partial z$ with height. Also indicated in Fig. 7a is the integrated condensation rate for the entire volume V of 40 kg s^{-1}. Of this total, 28 kg s^{-1} occurred below the 0°C level, while 12 kg s^{-1} occurred between the 0°C level and −4°C level.

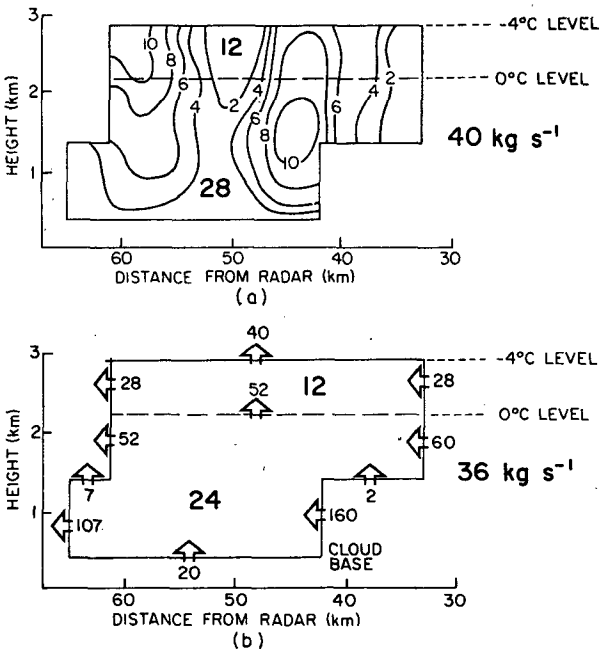

FIG. 7. Condensation rates in the warm-frontal rainband. a) Condensation rate (10^{-7} kg s^{-1} m^{-3}) calculated from the volume integral in a vertical plane oriented perpendicular to the width of the rainband. b) Vapor fluxes (kg s^{-1}) calculated from the surface integral across boundaries of the rainband for a 1 m length of the rainband normal to the cross section.

The total condensation rate below 3 km was calculated with the surface integral in (3) from fluxes of water vapor across various boundaries of the volume (Fig. 7b). The total condensation of 36 kg s^{-1} obtained this way agrees well with the value of 40 kg s^{-1} obtained from the volume integral. The vertical distribution of the condensation obtained with the surface integral, with 24 kg s^{-1} below the 0°C level and 12 kg s^{-1} between 0 and −4°C, also agrees well with the respective values of 28 kg s^{-1} and 12 kg s^{-1} obtained by the volume integral. Agreement between the volume and surface integral is expected since their values are obtained from the same basic data. The field of the integrand of the volume integral, however, provides a better visualization of the condensation pattern (Fig. 7a), while the various components of the surface integration (arrows in Fig. 7b) give a better visualization of the gross flow of water vapor into and out of the rainband.

As noted earlier, the velocities obtained from the Doppler radar above the 3 km level were unreliable. Consequently, direct calculations of the condensation rate above this level from radar data were not possible. To estimate this condensation, we note first that the aircraft data indicated the presence of generating cells between 4 and 5 km. However, it seems apparent from Fig. 2 that the generating cells probably extended somewhat above 5 km (note 24 dBZ contour). The region containing the generating cells is therefore assumed to extend from 4.0 to 5.5 km in our calculations. We assume further the pres-

ence of three precipitation fallstreaks emanating from these cells. The width of the observed fallstreaks (≈10 km) suggests that each streamer was fed by about three cells. Assuming this to be the case, nine cells, each 1.5 km in width and depth, were assumed to be located in the 4.0–5.5 km layer.

The combined condensation rate within the cells, obtained by applying (6) to their assumed volumes, range from 12 kg s^{-1} (using w = 50 cm s^{-1}) to 35 kg s^{-1} (using w = 150 cm s^{-1}). The estimate of vertical velocity in the generating cell were based on observations by Carbone and Bohne (1975).

In addition to the condensation within the cellular region (4–5.5 km altitude) and in the stratiform region (below 3 km), condensation evidently occurred in the intervening layer from 3 to 4 km. This was indicated by the presence of cloud liquid water in this region (Fig. 6). We can estimate the moisture condensed in this region by assuming an average vertical velocity within the layer and using (6). From Fig. 4a, the average vertical velocity across the 3 km level is 40 cm s^{-1}. If we assume the vertical velocity vanishes at echo top (≈6 km) and that the profile of the vertical velocity is linear in height throughout the layer from 3 to 6 km, values from 25 to 35 cm s^{-1} are obtained for the average vertical velocity in the layer from 3 to 4 km.

The various condensation rates from Fig. 7, computed by both the surface and volume integrals, are compared in Table 2 with measurements of the surface precipitation rate in the rainband.

The Pt. Brown raingage, located at the radar site, and the Moclips raingage, 34 km north-northwest of the radar, registered rainfall rates differing by a factor of 0.6. These measurements sampled different parts of the rainband and were obtained 30–45 min after the radar measurements on which the condensation calculations are based. It is difficult to say definitely which is more representative of the band at the time and location that it was detected with the radar. However, subjectively, the band became less well organized as it approached Moclips, perhaps explaining the lower surface precipitation rate at that site and suggesting that the Pt. Brown measurement is more representative of the band in its well-defined stage. The precipitation rate in Table 2, calculated from the CP-3 radar data, was obtained using the Z–R relationship of Marshall and Palmer (1948),

$$Z = 200R^{1.6}, \tag{7}$$

where Z is the radar reflectivity factor in $mm^6\ m^{-3}$ (dBZ = 10 $\log_{10}Z$) and R is the rainfall rate in mm h^{-1}. Drop-size data obtained with a distrometer at the radar site during the CYCLES PROJECT field phase of November–December 1976, were consistent with this relation. However, the CP-3 radar reflectivity values were found to be 4.3 dBZ low when checked against raingage data using (7) (J. W. Wilson, personal communication). Consequently, we increased the recorded reflectivities by this amount before applying (7). The surface precipitation rate of 58 kg s^{-1} thus obtained from the radar data in the rainband agrees well with the Pt. Brown raingage, further suggesting that it gave a more representative reading than the Moclips gage.

TABLE 2. Condensation and precipitation rates (kg s^{-1}) determined by various methods for the rainband. Condensation rates are for a 1 m length of the rainband.

Condensation below 3 km	
Surface integral	36
Volume integral	40
Average condensation below 3 km (C_1)	38
Condensation between 3 km and 4 km	
Volume integral	18–25
Condensation within cellular region (4–5.5 km)	
Volume integral	12–35
Total condensation (C)	68–98
Precipitation rate	
Moclips raingage	37
Pt. Brown raingage	62
Radar ($Z = 200R^{1.6}$)	58
Average precipitation rate (R)*	60
Efficiency ($\epsilon = R/C$)	60–90%

* Average rate from Pt. Brown gage and radar.

Considering the Pt. Brown gage and the radar rainfall measurements as the better indications of the surface rainfall rate of the rainband, we conclude from Table 2 that the precipitation rate R was ~60 kg s^{-1}, while the condensation rate below the 3 km level, C_1 was ~38 kg s^{-1} (the average value from surface and volume integral calculations). The remaining 22 kg s^{-1} of the precipitation must be explained by condensation that occurred above this level. From the estimates of the condensation above the 3 km level in Table 2, it is seen that the remaining 22 kg s^{-1} is more than accounted for by the condensation in the layer between 3 and 4 km and the cellular region between 4 and 5.5 km. From Table 2 we see that 0.65(= C_1/R) of the required condensation within the rainband occurred below the 3 km (or −4°C) level, with the remaining 0.35(= 1 − C_1/R) of the condensation occurring above the −4°C level.

Dividing the surface precipitation rate R from the rainband by the total condensation rate C within the rainband, a measure of the precipitation efficiency ϵ can be obtained. Values of ϵ derived from the data in the table range from 60 to 90%. The precipitation efficiencies for several rainbands studied during the CYCLES PROJECT have been presented by Hobbs *et al.* (1980). They found that wide cold-frontal rainbands, characterized by the "seeder-feeder" process, had efficiencies of 80 and 20%.

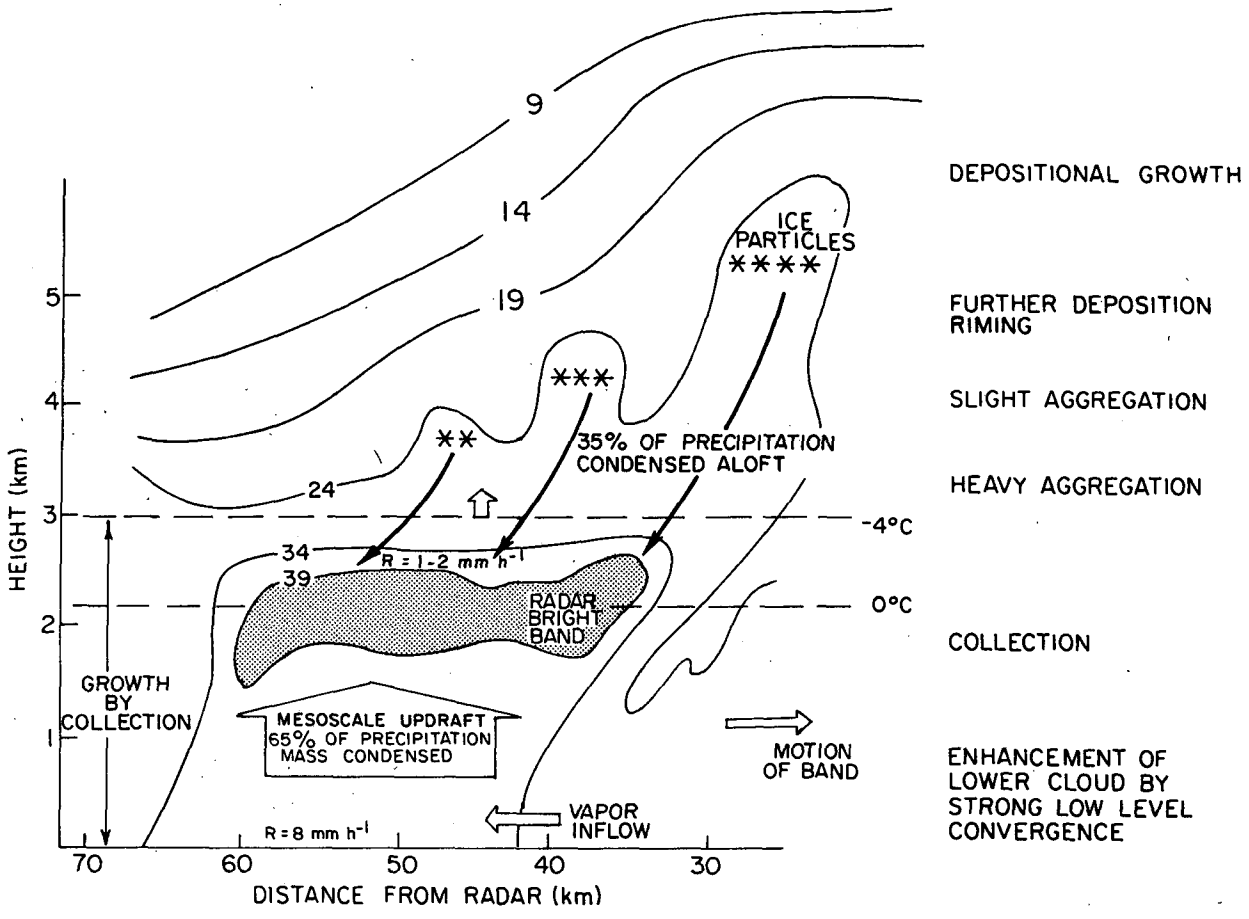

FIG. 8. Schematic illustration of the dynamical and microphysical precipitation processes associated with the warm-frontal rainband. Radar echo contours are taken from Fig. 2.

The latter value was for a band affected by strong low-level evaporation. The warm-frontal rainband of the present study, which also can be described as a seeder-feeder-type rainband, had an efficiency similar to the 80% value found by Hobbs *et al.* (1980) for the band that was not strongly affected by evaporation. In view of the inherent problems of representativeness of surface rainfall data and the computed vertical air motions, all these estimates of efficiencies must be interpreted with caution.

11. Conclusions

The warm frontal rainband in this study is illustrated schematically in Fig. 8. It was characterized at lower levels by a stratiform radar echo. Nearly uniform mesoscale lifting below the −4°C level led to the condensation of enough of the converged moisture to explain 65% of the surface precipitation that fell from the band. Above the −4°C level, moisture was condensed in convective cells overriding the stratiform echo region below.

Since the liquid droplets condensed below the −4°C level formed in a region of considerable horizontal wind relative to the rainband they were advected across the band at a rate that allowed an average of only 20 min for the particles to grow, which is probably an insufficient time for the particles to have reached precipitable sizes by either condensation (Mason, 1971, p. 124) or coalescence (Berry and Reinhardt, 1974). Hence, ice particles generated in the layer of convective cells aloft, falling into the layer below the −4°C level and aggregating just above the melting level were evidently crucial in converting the large amounts of water vapor condensing at low levels to precipitation by collecting it. The pronounced radar bright band associated with the rainband indicates that a large number of large ice particles were drifting down into the lower layer. Using the Z–R relationship for snow of Sekhon and Srivastava (1970), we find that the snowfall rates just above the melting level (corresponding to 30–40 dBZ) could have been no larger than 1–2 mm h^{-1}. Since surface rainfall rates were ≈8 mm h^{-1} (Table 2), it is evident that the scavenging of cloud water by the precipitation particles below the −4°C level was indeed substantial.

To summarize, Doppler radar and airborne cloud

microphysical observations indicate that the following key features were involved in enhancing the widespread cyclonic precipitation in the region of the observed warm frontal rainband. Ice particles were produced in shallow cells aloft, and underwent aggregation just above the melting level. As these particles accreted water droplets during their descent, they thus converted cloud water to precipitation (process 1 defined in Section 1). At low levels, enhanced mesoscale lifting produced a particularly dense stratiform cloud for the precipitation particles generated aloft to scavenge (process 2 in Section 1). This combination of mechanisms is essentially similar to the seeder-feeder process, first produced by Bergeron (1950) for orographic precipitation. The present results, however, emphasize the important role of the dynamics of the low-level feeder cloud. Mesoscale lifting present in the feeder cloud accounts for its ability to supply a sufficient amount of liquid water for the particles generated aloft to accrete as they descended. Future studies should be directed toward determining the dynamical origins of this key feature.

Acknowledgments. Thanks are due to all members of the University of Washington's Cloud Physics Group and to personnel from the National Center for Atmospheric Research's (NCAR) Atmospheric Technology Division for their valuable contributions to this study. The CYCLES PROJECT is supported by the Experimental Meteorology and Weather Modification Program, Division of Atmospheric Sciences, National Science Foundation (NSF) under Grants ATM74-14726-A02 and ATM77-01344, the Air Force Office of Scientific Research (Contract F49620-77-C-0057), the Environmental Research Laboratories of the National Oceanic and Atmospheric Administration (Grants 04-7023 and 44033), and the U.S. Army Research Office (DAAG 27-79-G-0005). The Doppler radar was provided by NCAR, which is sponsored by NSF.

REFERENCES

Battan, L. J., 1973: *Radar Observation of the Atmosphere.* University of Chicago Press, 324 pp.

Bergeron, T., 1950: Über der mechanismum der ausgeibigen Niederschläge. *Ber. Dtsch. Wetterdienstes*, **12**, 225–232.

Berry, E. X, and R. L. Reinhardt, 1974: An analysis of cloud drop growth by collection: Part I. Double distributions. *J. Atmos. Sci.*, **31**, 1814–1824.

Browning, K. A., and R. Wexler, 1968: The determination of kinematic properties of a wind field using Doppler radar. *J. Appl. Meteor.*, **7**, 105–113.

Carbone, R. E., and A. R. Bohne, 1975: Cellular snow generation—A Doppler radar study. *J. Atmos. Sci.*, **32**, 1384–1394.

Herzegh, P. H., and P. V. Hobbs, 1980: The mesoscale and microscale structure and organization of clouds and precipitation in mid-latitude cyclones. II: Warm-frontal clouds. *J. Atmos. Sci.*, **37**, 597–611.

Hobbs, P. V., 1974: *Ice Physics.* Oxford University Press, 837 pp.

——, and J. D. Locatelli, 1978: Rainbands, precipitation cores and generating cells in a cyclonic storm. *J. Atmos. Sci.*, **35**, 230–241.

——, T. J. Matejka, P. H. Herzegh, J. D. Locatelli and R. A. Houze, Jr., 1980: The mesoscale and microscale structure and organization of clouds and precipitation in midlatitude cyclones. I: A case study of a cold front. *J. Atmos. Sci.*, **37**, 568–596.

Holton, J. R., 1972: *An Introduction to Dynamic Meteorology.* Academic Press, 319 pp.

Houghton, H. G., 1950: A preliminary quantitative analysis of precipitation mechanisms. *J. Meteor.*, **7**, 363–369.

Houze, R. A., Jr., J. D. Locatelli and P. V. Hobbs, 1976a: Dynamics and cloud microphysics of the rainbands in an occluded frontal system. *J. Atmos. Sci.*, **33**, 1921–1936.

——, P. V. Hobbs, K. R. Biswas and W. M. Davis, 1976b: Mesoscale rainbands in extratropical cyclones: *Mon. Wea. Rev.*, **104**, 868–878.

Marshall, J. S., and W. McK. Palmer, 1948: The distribution of raindrops with size. *J. Meteor.*, **5**, 165–166.

Mason, B. J., 1971: *The Physics of Clouds.* Oxford University Press, 671 pp.

Matejka, T. J., R. A. Houze, Jr., and P. V. Hobbs, 1980: Microphysics and dynamics of the clouds associated with mesoscale rainbands in extratropical cyclones. *Quart. J. Roy. Meteor. Soc.*, **106**, 29–56.

Sekhon, R. S., and R. C. Srivastava, 1970: Snow size spectra and radar reflectivity. *J. Atmos. Sci.*, **27**, 299–307.